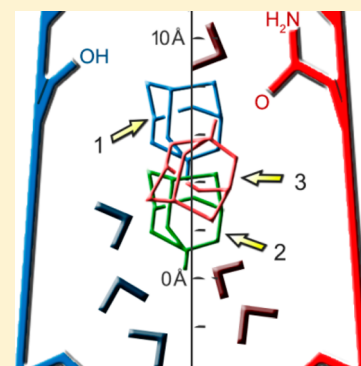


# Resistance-Mutation (N31) Effects on Drug Orientation and Channel Hydration in Amantadine-Bound Influenza A M2

Mitchell L. Gleed,<sup>†</sup> Harris Ioannidis,<sup>‡</sup> Antonios Kolocouris,<sup>‡</sup> and David D. Busath<sup>\*,†</sup><sup>†</sup>Department of Physiology and Developmental Biology, Brigham Young University, Provo, Utah 84602, United States<sup>‡</sup>Department of Pharmaceutical Chemistry, Faculty of Pharmacy, National and Kapodistrian University of Athens, Athens, Greece

## S Supporting Information

**ABSTRACT:** The mechanism of amantadine binding to the S31 variant of the M2 protein of Influenza A is well understood, but the reasons behind N31 M2 amantadine insensitivity remain under investigation. Many molecular dynamics studies have evaluated the influence of amantadine position within the channel pore on its ability to inhibit proton conductance in M2, but little is known about the influence of amantadine rotational orientation. Replica-exchange umbrella sampling, steered, and classic molecular dynamics simulations were performed on amantadine in the solid-state NMR structure of S31 M2 and an N31 M2 homologue, both in the homotetramer configuration, to explore the effects of the position and tilt angle of amantadine on inhibition of the M2 channel. Steered simulations show that amantadine rotates with the amine toward the bulk water as it passes into the hydrophobic entryway lined by Val27 side chains. Results from all simulation types performed indicate that amantadine has a strong, specific orientation with the amine turned inward toward the central cavity in the S31 M2 pore but has variable orientation and a strong propensity to remain outward pointing in N31 M2. Free energy profiles from umbrella sampling, measured relative to bulk water, show amantadine binds more strongly to the S31 M2 pore by 8 kcal/mol in comparison to amantadine in the N31 pore, suggesting that it can escape more readily from the N31 channel through the Val27 secondary gate, whereas it is captured by the S31 channel in the same region. Lower water density and distribution near amantadine in S31 M2 reveal that the drug inhibits proton conductance in S31 M2 because of its inward-pointing configuration, whereas in N31 M2, amantadine forms hydrogen bonds with an N31 side chain and does not widely occlude water occupancy in any configuration. Both amantadine's weaker binding to and weaker water occlusion in N31 M2 might contribute to its inefficacy as an inhibitor of the mutant protein.



## ■ INTRODUCTION

Influenza A is a notorious virus responsible for producing severe illness resulting in the hospitalization of millions throughout the world every year despite significant efforts to reduce influenza infection by vaccination. Influenza outbreaks vary in mortality and reach, occasionally reaching pandemic levels. In 2013, influenza, combined with pneumonia, was the eighth leading cause of death in the United States.<sup>1</sup> Finding suitable antiviral drugs to treat influenza infection, particularly with the highly prevalent, amantadine-insensitive M2 (S31N), is a key field of influenza research, and M2 protein inhibitors are a significant class of anti-influenza agents.<sup>2–6</sup>

The M2 proton channel of Influenza A is a critical protein in the viral replication cycle. When proton transport through the channel is inhibited, the cycle is arrested and infection of the host is halted. Adamantane-variant compounds amantadine and rimantadine were once effective inhibiting Influenza A M2, but recent strains, such as seasonal H3N2, which typically feature an S31N M2 mutant, are resistant to these compounds, which are consequently no longer recommended for influenza treatment in the United States.<sup>7</sup>

The reasons why adamantanes inhibit proton conductance in S31 (wild type) M2, but do not affect N31 Influenza A M2, have been the subject of many computational investigations. In

a previous work, we determined that amantadine lacks locational specificity when simulated in the transmembrane domain of N31 M2, compared to the tighter, more-specific binding region observed in simulations of the wild-type protein.<sup>8</sup> Some have suggested that the increased steric hindrance of the S31N mutation causes adamantanes to lose stability in the region.<sup>9</sup> Others have shown that binding affinity of adamantanes in S31 M2 depends largely on each drug's hydrogen-bonding ability, electrostatic and van der Waals interactions, and energy of desolvation upon M2 pore entry.<sup>10</sup> Additionally, the importance of drug amine location in the channel<sup>3,11–13</sup> and water structure around the drug<sup>14</sup> have been highlighted. In particular, amine binding sites near the backbone carbonyls of residues 27, 31, and 34 have been identified as possibly relevant for binding of adamantanes in S31 and N31 M2.<sup>3</sup>

The position of amantadine in M2 is a key aspect to consider when evaluating its antiviral efficacy. In molecular dynamics (MD) simulations of the high-resolution X-ray structure of homotetrameric S31 M2 [PDB ID: 3LBW],<sup>15</sup> Gianti et al.

Received: June 17, 2015

Revised: August 10, 2015

Published: August 13, 2015

(2015)<sup>14</sup> identified prominent free energy minima for the amine of amantadine in the central cavities of S31 and N31 M2—near the alpha carbons of Gly34 in S31 M2 and slightly C-ward to the alpha carbons of Asn31 in N31 M2. Our previous free energy profiles from the umbrella sampling of amantadine in the ssNMR structure of amantadine-bound M2 [PDB ID: 2KQT]<sup>16</sup> showed that the adamantane cage of amantadine tends to stay between residues 31 and 34 in both the native structure and its S31N homologue.<sup>8</sup> However, the free energy profiles differed significantly in both magnitude and location of free energy minima/maxima depending on the amantadine starting orientation, resulting in high standard deviations in the free energy profiles when the potentials of mean force (PMF) from all starting orientations were averaged. Consequently, we found the influence of amantadine orientation must also be taken into consideration.

Structural<sup>17</sup> and computational studies<sup>18,19</sup> have shown that amantadine tends to orient in the S31 M2 pore with its amine oriented toward the protein C-terminus when the His37 residues are neutral, but little work has been done to shine light on the orientation of amantadine in N31 M2. In some of our initial simulations of the N31 M2 homologue in unrestrained MD simulations with amantadine initiated in the NMR binding site for the S31 M2 channel,<sup>16</sup> amantadine moved deeper into the wider part of the channel by  $\sim 2$  Å within the first 9 ns and rotated almost half a turn such that, for a large portion of the run ( $\sim 30$  ns), its amine group projected toward the N-terminus and hydrogen bonded with the side chains of N31 and water molecules in the vicinity. In contrast, when amantadine was initiated in the same site but with the amine rotated such that it pointed out of the S31 channel instead of into it, amantadine rapidly ( $< 10$  ns) rotated back to the opposite configuration, i.e., the NMR position with the amine group pointed into the channel and retained that orientation for the remainder of the simulation (Figure 1).

Computational studies of M2 have commonly investigated free energies of various antiviral compounds with methods such as umbrella sampling<sup>8,20</sup> and metadynamics.<sup>14</sup> However, to this point, they have been limited to exploring a single dimension—the position of the compounds along the bilayer normal in M2. The observation that amantadine adopts different primary orientations between S31 and N31 M2 spurs many important questions, such as the following: Are certain amantadine orientations energetically favorable? Which amantadine orientations most effectively inhibit proton transport? What role does orientation play in amantadine insensitivity of N31 M2?

To better understand the influence of amantadine orientation in M2 inhibition, we explore not only its position but also its orientation with respect to the channel axis in the Influenza A M2 transmembrane domain (M2TM) using 2-dimensional umbrella sampling replica-exchange, steered, and classic molecular dynamics simulations. The principal amine binding positions identified by Wang et al. (2013)<sup>3</sup> are seen to play an important role for amantadine binding with the positions at carbonyls 31 and 34 being key to amantadine binding in S31 and the position at carbonyl 27 (which is also near the plane of the N31 side chain carbonyls) having an important, perhaps kinetic, role for amantadine binding in N31. Our results demonstrate that amantadine orientation and amantadine binding affinity play important roles in both its ability to inhibit S31 M2 and inability to inhibit N31 M2. In particular, an outward facing configuration is persistent in steered MD simulations with N31 M2 due to hydrogen bonding with the

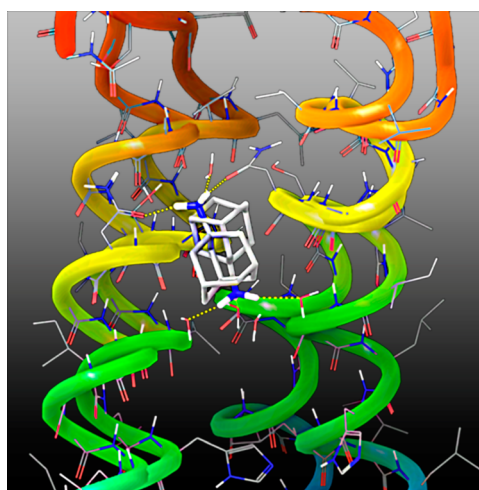


**Figure 1.** Amantadine orients toward the protein C-terminus in S31 M2 and toward the protein N-terminus in N31 M2. Superposition of final snapshots from Desmond2012/OPLS2005 of constant-temperature and -pressure molecular dynamics simulations at 310 K of amantadine in complex with S31 or N31 M2 [PDB ID: 2KQT] in 150 mM NaCl, water, and a DMPC lipid bilayer (Figure S1). Two of four M2 transmembrane-domain backbones are shown as tubes with coloration varying from the N-terminus (red) to the C-terminus (cyan). In the S31 case, the amantadine amine is projecting toward the C-terminus and hydrogen bonding with two water molecules. In the N31 case, the adamantane cage (gray) is lower, and the amantadine amine projects toward the N-terminus and hydrogen bonds with the two N31 side chains and a water molecule. In the starting structure for N31 M2, Asn31 side chains were initially placed at the interface between helices ( $\chi_1 \approx -160^\circ$ ) but moved within  $\sim 20$  ns to the final luminal projections ( $\chi_1 \approx -90^\circ$ ) shown here.

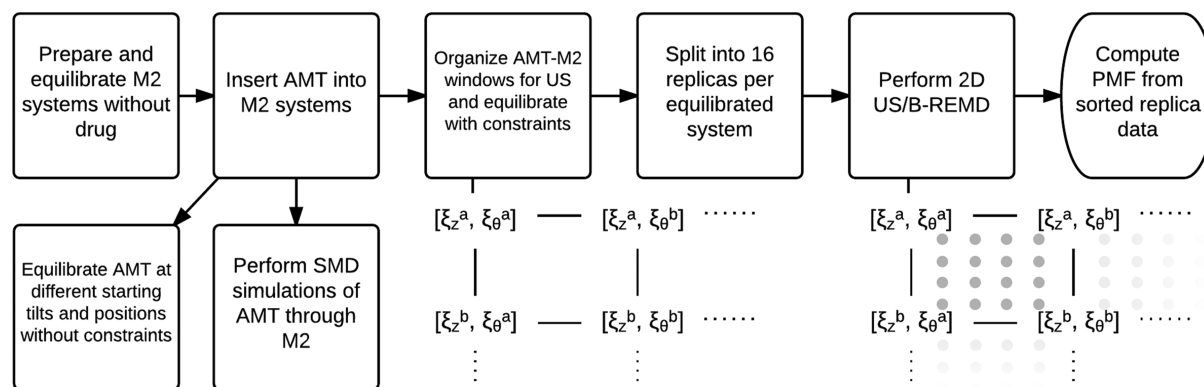
N31 side chain carbonyls. Careful evaluation of the water density around the drug shows here that binding in the channel without block is less likely than previously suggested.<sup>8</sup> Rather, the 2D free energy topologies determined here indicate that weak binding in the N31 channel could be the principal reason for weak block.

## METHODOLOGY

The ssNMR structure by Cady et al. (2010) [PDB ID: 2KQT]<sup>16</sup> was chosen to model M2TM in the neutral pH blocked state, as well as to serve as a template in the creation of a homology model of the prevailing M2 mutant S31N. Cationic amantadine (AMT) was used for all simulations in the study for reasons given previously.<sup>8</sup> All phases of simulation employed the current CHARMM36 force field parameters to describe proteins and lipids,<sup>21,22</sup> and the TIP3P model was chosen to represent water.<sup>23</sup> AMT topology and parameters were generated by analogy based on adamantane parameters from the CHARMM General Force field (CGenFF) version 36<sup>24,25</sup> using ParamChem.<sup>26,27</sup> In simulations, long-range Coulombic interactions were calculated using the particle mesh Ewald (PME) algorithm,<sup>28</sup> the Shake method was used to keep all bonds with hydrogen rigid at ideal lengths and angles,<sup>29</sup> and short-range electrostatic and van der Waals forces were smoothed using a switching distance of 11 Å. Matlab R2014b was used to visualize trajectory data and generate contour images. The cubehelix color map was used to color contour plots.<sup>30</sup>

We use a two-dimensional reaction coordinate,  $\xi$ , for AMT translocation through M2TM. The first component,  $\xi_z$ , is the

Scheme 1. Summary of the Simulation Protocol



displacement of the center of mass of the adamantane cage of AMT along the  $z$  axis (approximately the bilayer normal), expressed in Å.  $\xi_z = 0$  Å is at the origin of the simulation system, which is approximately the center plane of the bilayer. The second component,  $\xi_\theta$  is the angle formed between the  $x$ - $y$  plane and the vector passing through the adamantane center of mass and  $\text{NH}_3^+$  of AMT with  $\pm 90^\circ$  as perpendicular to  $x$ - $y$ . We describe AMT as outward facing (or N-ward facing when in the M2TM pore) when  $\xi_\theta \geq 45^\circ$  and inward facing (or C-ward facing when in the M2TM pore) when  $\xi_\theta \leq -45^\circ$ . The computational protocol is summarized in Scheme 1 and is described in the following paragraphs.

**M2TM Structure Preparation.** M2TM structures were hydrated and inserted into lipid membranes for simulations using the CHARMM-GUI Membrane Builder.<sup>31,32</sup> All ssNMR PDB models were imported from the RCSB database at PDB.org. His37 residues were each assigned a proton at the  $\text{N}\epsilon$ <sup>33</sup> site but not at the  $\text{N}\delta$  site as would be expected when an adamantane compound is bound,<sup>34,35</sup> and protein termini were charged amino and carboxylate groups. An N31 homologue structure was generated in the same manner with serine mutated to asparagine for each protein monomer at position 31. After both S31 and N31 structures were generated, they were each placed into a hydrated DMPC bilayer (to agree with NMR conditions used in the structural determination<sup>16</sup>) using the insertion method and oriented according to the Orientations of Proteins in Membranes (OPM) database.<sup>36</sup> Channel pore waters were also generated using CHARMM-GUI, and  $\text{Na}^+$  and  $\text{Cl}^-$  ions were added to each system by Monte Carlo placement for an electroneutral system at an ion concentration in the bulk of  $\sim 0.15$  M. The systems generated consisted of the M2TM protein (S31 or N31), 94 DMPC lipids, and over 5,000 TIP3 water molecules in unit cells of approximately  $60 \times 60 \times 72$  Å<sup>3</sup> in the  $x$ ,  $y$ , and  $z$  dimensions.

**Initial Equilibration without AMT.** Initial minimization and equilibration of S31 and N31 systems, following their creation in CHARMM-GUI, was performed using CHARMM version 37b1.<sup>37</sup> The protein coordinates of all of the 17 models in 2KQT obtained from NMR refinement were averaged, and these coordinates served to restrain protein backbone atoms during simulation. Several rounds of minimization were applied to adapt the systems to the CHARMM36 force field, after which seven phases of equilibration were performed, with weakening harmonic restraints for each consecutive phase. Langevin temperature control was used to bring the systems to and hold them at 310 K for the first 50 ps, after which the Hoover thermostat and extended-system algorithm were used

to hold the systems near 310 K and 1 atm for the remainder of the equilibration. The simulation temperature was chosen to be above the gel to liquid-crystalline phase transition temperature of  $\sim 297$  K for DMPC.<sup>38</sup> The systems were equilibrated, in the final phase, for 20 ns each with a 2 fs time step and a 0.1 kcal/mol-Å<sup>2</sup> harmonic restraint on each protein backbone atom.

**Two-Dimensional Umbrella Sampling with Replica Exchange.** The free energy landscape, or potential of mean force (PMF), of AMT in S31 and N31 M2TM systems was explored using 2-dimensional umbrella sampling enhanced with replica-exchange molecular dynamics (US/REMD) in NAMD 2.10.<sup>39</sup> To avoid any undesired effects that might occur with excessive temperatures in the sensitive DMPC bilayer environment, we implemented a Hamiltonian replica-exchange scheme, rather than a parallel-tempering scheme, for the present study, analogous to that of Murata et al. (2014)<sup>40</sup> in which biasing parameters of adjacent replicas are exchanged according to a Metropolis energy criterion rather than atom velocities. With this method, we are able to sample the orthogonal degrees of freedom that are unlikely to be fully sampled on a short time scale. Our implementation is adapted from the *umbrella2d* protocol in the NAMD 2.10 source tree.

Using the collective variables module,<sup>41</sup> we applied harmonic restraints to  $\xi_z$  and  $\xi_\theta$ . Applied harmonic restraint penalties include 25 kcal/mol-Å<sup>2</sup> to deviations from set point in  $\xi_z$ , 100 kcal/mol-(cos units)<sup>2</sup> to the deviation from set point in  $\cos(90^\circ + \xi_\theta)$ , and 10 kcal/mol-Å<sup>2</sup> to the deviation of protein backbone center of mass from the original position, and the backbone heavy atom root-mean-square deviation (RMSD) from the average backbone coordinates of the 2KQT models. Separate simulations were performed at intervals of  $\xi_z = 1$  Å, from  $-25$  to  $25$  Å, and  $\cos(90^\circ + \xi_\theta) = 0.2$ , from 1 (parallel) to  $-1$  (antiparallel) with respect to the  $+z$  axis. Cosine( $\theta$ ) space, rather than  $\theta$  space, was sampled in order to compensate for the increased availability of positions near  $\theta = 0$ . The results can thus be interpreted in terms of the mean force of rotation (as opposed to the free energy profile relevant to the kinetics of rotation).

For each umbrella window, AMT was placed and oriented according to a unique combination of  $\xi_z$  and  $\xi_\theta$ , after which the simulation system was equilibrated for 1 ns. Following equilibration of AMT, each umbrella window was simulated using 16 parallel replicas, each of which was assigned a specific, unique combination of bias locations for  $\xi_z$  and  $\xi_\theta$  for 1 ns each. Neighboring replicas differed in bias location by  $\xi_z = 0.25$  Å or by  $\cos(90^\circ + \xi_\theta) = 0.05$ , and exchanges were attempted every 1000 MD steps (2 ps) and accepted if the Metropolis criterion

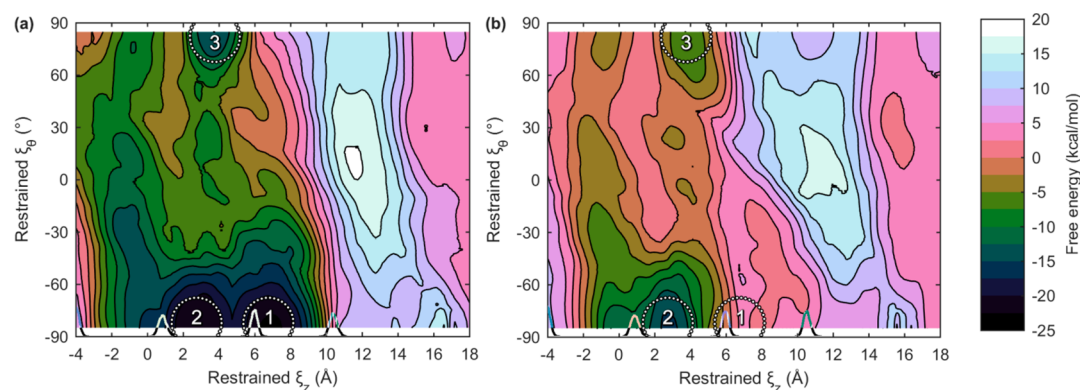


**Figure 2.** Two-dimensional free-energy topology for AMT in the M2TM central cavity. The 2-dimensional PMF of AMT in (a) S31 and (b) N31 M2TM systems from US/REMD simulations. Contours are drawn with 2.5 kcal/mol separations. The free energy at the simulation extremes (AMT in bulk water, see Figure S5) is set to 0 kcal/mol. Relative average C- $\alpha$  mass densities from apo-M2 equilibration trajectories (histograms) of residues Val27, Ser/Asn31, Gly34, and His37 are shown for reference from right to left at the base of the plots. Data near the  $-90^\circ$  and  $90^\circ$  extremes are absent due to the binning of  $\cos(90^\circ + \xi_\theta)$  for WHAM with subsequent conversion to degrees for the PMF. Three key AMT configurations are identified with numbered circles.

was satisfied. The implementation of collective variables, replica exchange, and 2D-weighted-histogram analysis method (WHAM) analysis was validated with a model system consisting of an AMT molecule and a  $\text{Cl}^-$  ion (Figure S2).

**Steered Molecular Dynamics.** Steered MD is a method commonly used to explore the free energy profile of a compound in a system of interest. Rather than use steered MD to compute the PMF of AMT in M2TM—which is based on linear rather than variable kinetics of AMT passage—we used steered MD to explore the behavior of AMT upon M2TM entry and observe any changes in orientation. Steered MD simulations were performed using NAMD's collective variables module<sup>41</sup> to drive AMT through S31 and N31 M2TM with a restraint on  $\xi_z$ . Equilibrated systems without AMT, created as described previously, were read into NAMD, and AMT was placed in a fully solvated configuration with a starting position of 30 Å on the  $z$  axis (distant from M2TM and the lipid bilayer). Harmonic restraints of 25 and 10 kcal/mol-Å<sup>2</sup> were applied to  $\xi_z$  and protein backbone atoms, respectively. Five independent simulations of varying initial velocities were performed for both S31 and N31 M2TM systems for 200 ns each (2 fs time step), in which AMT was moved from 30 to  $-30$  Å along the  $z$  axis, resulting in a velocity of  $d\xi_z/dt = 0.3$  Å/ns. The collective variable  $\xi_\theta$  was unrestrained, and time series data for  $\xi_z$  and  $\xi_\theta$  were measured every 200 fs. Using Matlab, the rational-transfer function *filter* was used to apply a moving average over 1 million time-series samples per simulation trajectory, with a window size of 50 and denominator coefficient of 1, in order to improve figure clarity. As a metric of interruption of Grotthus proton conductance by AMT, the minimum  $z$  value for all water oxygens with  $z > \xi_z$ , and the maximum  $z$  value for all water oxygens with  $z < \xi_z$  were extracted for each stored frame, and the latter value was subtracted from the former to obtain a drug-induced water separation distance.

**Configuration Sampling of AMT in M2TM.** We studied the relaxation to equilibration positions and orientations of AMT within S31 and N31 M2TM by allowing AMT to relax toward equilibrium configurations from different initial positions and orientations. The relaxation trajectories for  $\xi_z$  and  $\xi_\theta$  were studied by positioning AMT between  $-4$  and  $10$  Å on the  $z$  axis in intervals of  $\xi_z = 0.25$  Å and orienting AMT

from  $90^\circ$  to  $-90^\circ$  in intervals of  $\xi_\theta = 30^\circ$ . Structures were prepared, waters overlapping AMT deleted, and systems minimized with CHARMM, after which heating and production dynamics were performed in NAMD at each initial AMT configuration for 5 ns of simulation time for each of three independent runs of varying initial velocities. Collective variable data for  $\xi_z$  and  $\xi_\theta$  were captured every 200 fs. A harmonic restraint of 0.1 kcal/mol-Å<sup>2</sup> was applied to the protein backbone center of mass and root-mean-square deviation (RMSD). To determine the stability of AMT in its most prominent configurations and the occlusion of water by AMT on a longer time scale, two simulations were extended for an additional 200 ns without restraints: one in S31 and the other in N31 M2TM.

## RESULTS

**Apo-M2 Hydration.** Equilibration of M2 channels without drug present showed nearly equivalent RMSD ( $\sim 0.5$  Å) and water content ( $\sim 20$  lumenal molecules) for S31 and N31 M2TM. Consequently, we considered any significant deviations in water content, volume density, or molecular separation that were observed between M2TM channels in further experiments to result directly from controlled variables. Data for center-of-mass  $z$  position and RMSD of each residue, water content, and water density of each channel are shown in Table S1 and Figures S3–S5.

**US/REMD Simulations.** Following the 2-dimensional US/REMD simulations, replica trajectories and collective variable data were resorted according to each replica's combination of  $\xi_z$  and  $\xi_\theta$ . The average exchange acceptance ratio over all umbrella windows and both channel types was  $\sim 0.49$  ( $s = 0.23$ ). The weighted-histogram analysis method (WHAM),<sup>42</sup> with periodicity in  $\xi_z$  for AMT in bulk water, was used to compute the potential of mean force (PMF) of AMT in S31 and N31 systems using collective variable data from the resorted simulation time-series data. The PMFs for both systems are shown in Figure 2. Full-range PMFs, as well as analysis of water content from the sorted replica trajectories of the US/REMD simulations, are found in Figures S6 and S7.

We identified three significant AMT configurations from the free energy minima in the PMFs. Two minima were present in both PMFs at  $1 \text{ \AA} \leq \xi_z \leq 4 \text{ \AA}$ ,  $\xi_\theta \geq 60^\circ$  (C3) and  $2 \text{ \AA} \leq \xi_z \leq 5$

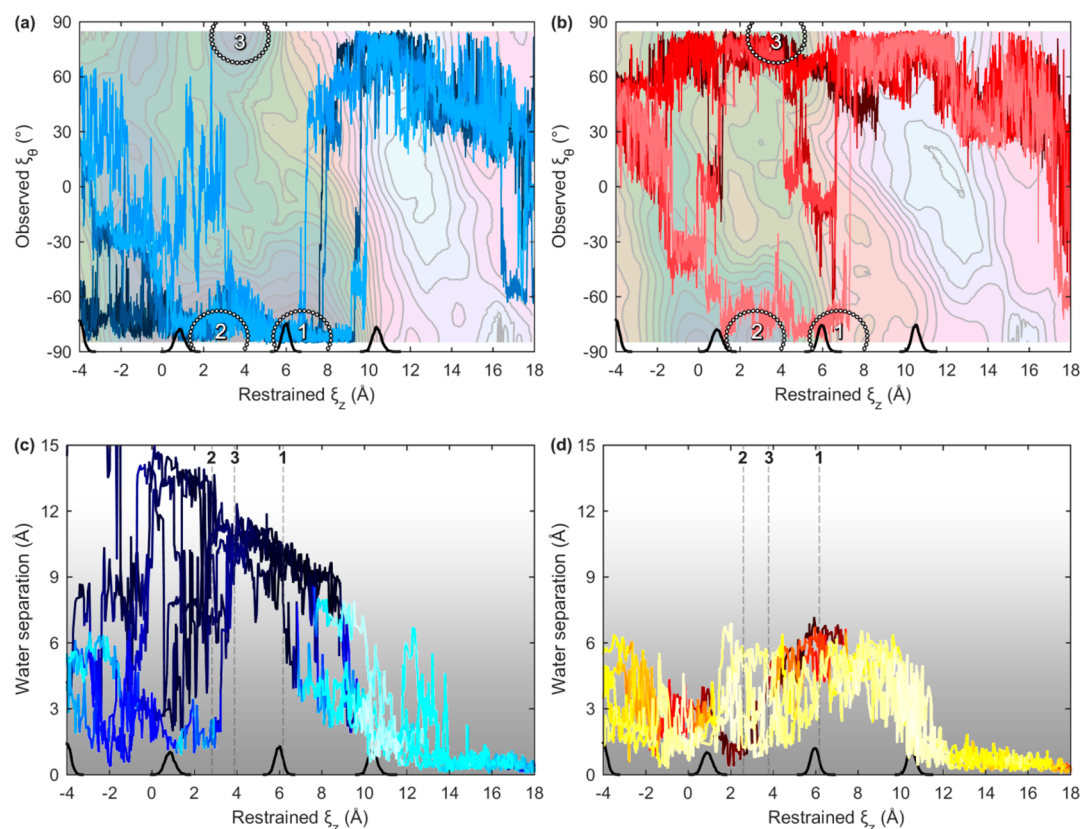


**Figure 3.** AMT orientation in M2 and ability to cleave water according to steered MD simulations. Steered MD simulations reveal  $\xi_\theta$  (a, b) and separation of water molecules (c,d), i.e., the minimal distance between water atoms above and below AMT), varies as  $\xi_z$  is slowly translated C-ward through M2TM from bulk water to the His37 cluster in S31 (a, c) and N31 (b, d) channels in each of five simulations for each channel. In (a) and (b), each run is drawn with a unique trace color, the US/REMD PMFs are replicated in the background, and representative regions of C1, C2, and C3 are indicated by numbered circles. In (c) and (d), each trace is colored by  $\xi_\theta$  with dark and light coloration representing C- and N-ward facing AMT, respectively, and the highest-occupancy regions in  $\xi_z$  near C1, C2, and C3 from the configuration-sampling study (see Figure 6) are shown with dashed lines. C- $\alpha$  mass densities from apo-M2 equilibration trajectories (histograms) of residues Val27, Ser/Asn31, Gly34, and His37 are shown for reference from right to left in all plots.

Å,  $\xi_\theta < -60^\circ$  (C2). A third minima, exclusive to the S31 PMF, is found at  $5 \text{ \AA} \leq \xi_z \leq 8 \text{ \AA}$ ,  $\xi_\theta < -70^\circ$  (C1). Positions C1 and C2 have the  $\text{NH}_3^+$  of AMT pointing inward and near the carbonyl planes for residues 31 and 34, respectively. Position C3 has the  $\text{NH}_3^+$  pointing outward and near the carbonyl plane for residue 28. In S31 M2TM, C1 and C2, both inward-facing configurations, have free energies of  $-23.5$  and  $-22$  kcal/mol relative to bulk water; and C3, the outward-facing configuration, has a free energy of  $-15$  kcal/mol. In N31 M2TM, the free energies of C2 and C3 are  $-15.5$  and  $-7.3$  kcal/mol, respectively. Relative to bulk water, AMT binds to S31 better than N31 M2TM by a global free-energy difference of  $\sim 8$  kcal/mol.

**Steered MD Simulations.** Simulations carried out with a moving restraint that steers AMT along  $\xi_z$  into the N-terminus show the specific orientations assumed by AMT as it passes into the channel and the influence of  $\xi_z$  and  $\xi_\theta$  on the AMT-induced separation of water molecules. The variations in  $\xi_\theta$  and water separation with  $\xi_z$  are shown in Figure 3.

AMT invariably backs into the channel adamantane-first as the restraint on  $\xi_z$  moves from 16 to 10 Å. In S31 M2TM (Figure 3a), AMT flips so that its  $\text{NH}_3^+$  group faces the His37 selectivity filter after it passes the Val27 side chains (7–10 Å) and maintains an inward-pointing orientation within the central cavity (3–7 Å). For N31 (Figure 3b), AMT starts to turn toward the C-terminus at 6–7 Å for three trajectories but

returns to an outward-pointing orientation at 5 Å in two and remains inward-pointing in only one. In the other two trajectories, it stays outward pointing throughout the passage in the central cavity (1–10 Å). The observation that AMT backs in is consistent with the expectation that the hydrophobic adamantane would be best coordinated by hydrophobic Val27 side chains, while the hydrophilic  $\text{NH}_3^+$  of AMT would strongly interact with bulk electrolyte. However, because this structure lacks the N-terminus of the full protein, the entry process may not reflect that of native protein. Likewise, the complete flipping after entry in all five AMT trajectories in S31 and one in N31 is consistent with the probable attraction of the  $\text{NH}_3^+$  of AMT to intrachannel water molecules. A diagonal ridge in the free energy profile for AMT in N31 from (10 Å,  $0^\circ$ ) to (5 Å,  $40^\circ$ ) begins to explain the propensity for AMT to remain outward pointing in N31. We further evaluate this observation in the Discussion.

As with the 2D umbrella-sampling water densities (Figure S7), water separation is most extreme ( $>10$  Å) and robust (low in S.D.) for the steered MD runs in the S31 channel (Figure 3c) when  $4 \text{ \AA} \leq \xi_z \leq 6 \text{ \AA}$ , where AMT adopts an inward-facing orientation. For the same region of the transport coordinate for the N31 channel (Figure 3d), the propensity for AMT to face inward is modest, and the average water separation is small ( $<6$  Å), suggesting a weak capacity for bound AMT to block N31 M2TM.

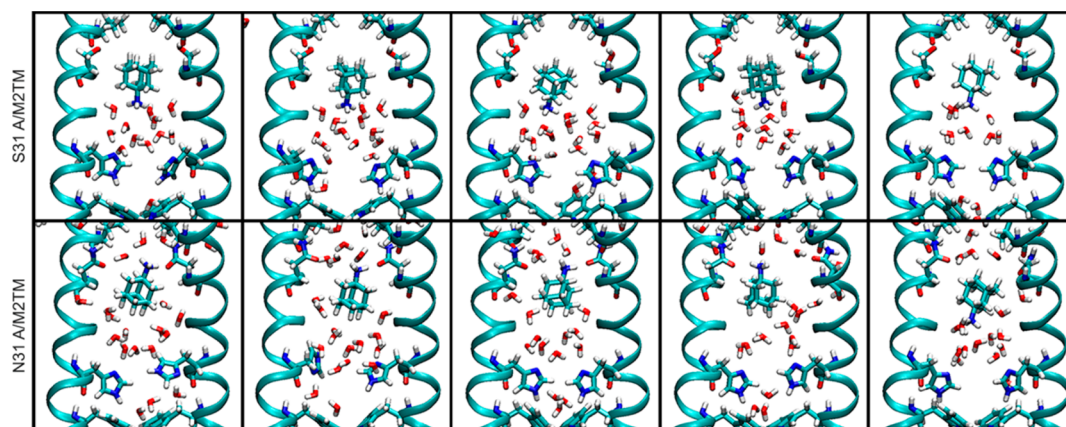


**Figure 4.** Snapshots of AMT orientations in S31 and N31 M2TM. Five unique steered MD simulation trajectories with AMT restrained to near  $\xi_z = 4.0$  Å are shown here for S31 (top) and N31 (bottom) M2TM systems. Protein backbones are shown in ribbons, and residues Val27, Ser/Asn31, His37, and Trp41 are shown as sticks from top to bottom, respectively.

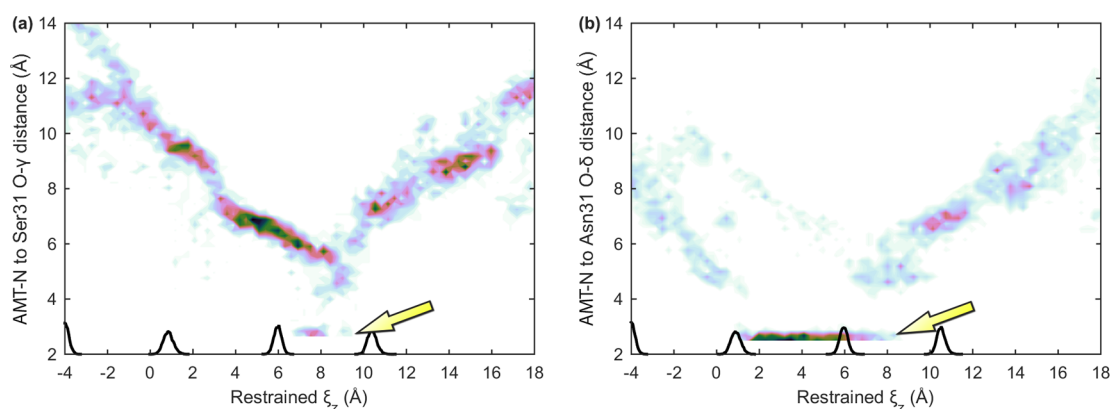


**Figure 5.** AMT hydrogen bonding to the side chain of residue 31. The minimum distance between the AMT N and the nearest (a) Ser31 O- $\gamma$  or (b) Asn31 O- $\delta$  varies with  $\xi_z$  in M2TM simulations. An AMT N to Ser/Asn31 O distance of 2.5–3 Å is indicative of hydrogen bonding. Increasing pair density is represented by darker color intensity. Relative average C- $\alpha$  mass densities from apo-M2 equilibration trajectories (histograms) of residues Val27, Ser/Asn31, Gly34, and His37 are shown from right to left for reference. Superimposed arrows indicate regions in which hydrogen bonding is observed.

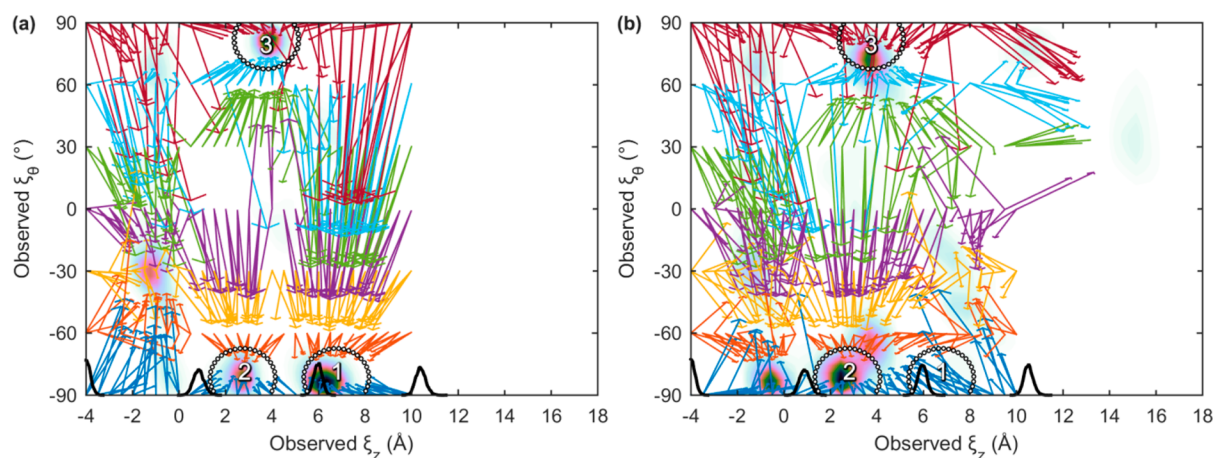


**Figure 6.** Relaxation in drug position and orientation for different starting configurations. Unrestrained AMT relaxation for (a) S31 and (b) N31 M2TM in separate 5 ns simulation systems. Increasing AMT occupancy is designated with darker color intensity. Arrows, superimposed and colored by starting AMT tilt, originate at each AMT starting configuration and extend half the distance to the average AMT configuration adopted in the last 1 ns for each of three independent runs of varying initial velocities. Relative average C- $\alpha$  mass densities from apo-M2 equilibration trajectories (black histograms) are shown for residues Val27, Ser/Asn31, Gly34, and His37 from right to left. Representative regions of C1, C2, and C3 overlay the plots (numbered circles).

To illustrate, we show representative trajectory snapshots from the steered MD runs of AMT restrained near  $\xi_z = 4$  Å, just slightly N-ward of C3 and C2, in Figure 4. In all five cases for S31 (top row), AMT faces the His37 cluster, and no water molecules are found above or alongside the drug. In four of five cases for N31 (bottom row), AMT faces outward and, in all five cases, water molecules are found above and alongside the drug. In all four outward-facing configurations, the AMT is hydrogen bonded to the CO of an N31 side chain.

To investigate the influence of hydrogen bonding of Ser31 and Asn31 side-chain oxygen atoms to the aminium nitrogen of AMT, we measured the distances between the two atoms for all frames of each steered MD run. For each frame, the minimum distance was used such that the longer distances to the same residue in other subunits were excluded. The density of “N–O distance” pairs in each pixel is shown by a color (white = 0) as a function of adamantane center of mass position  $\xi_z$  for S31 and N31 M2TM systems in Figure 5.

There is a strong density of hydrogen bonds for AMT in N31 when the drug center of mass is located in the central cavity, between 2 and 7 Å. The density is much smaller and limited to a narrow range of 7–8 Å for the S31 channel. Furthermore, hydrogen bonds with the Asn31 side chain are associated with a more vertical, outward-facing AMT orientation, which we propose is enhanced by the greater extension of the side chain into the channel (see Figure 4). Perhaps both acceptor accessibility and interaction strength contribute to the strong hydrogen bonding of AMT to N31. To the extent that the force field is accurate, we conclude that AMT hydrogen bonds very strongly with the N31 side chain carbonyl in this structure, as demonstrated by the high occupancy of the hydrogen-bonded state, and propose that this interaction is an important factor in holding AMT outward-facing in the N31 M2TM channel. We also find that hydrogen bonding influences  $\xi_\theta$  when we compare the observed  $\xi_\theta$  to the distances between AMT N and residue 31 side-chain oxygen for all steered MD frames in which  $2 \text{ Å} \leq \xi_z \leq 8 \text{ Å}$ ; these results are found in Figure S8.

**Configuration Sampling Simulations.** To observe the relaxation of AMT in the pore region of M2TM (between the Val27 and His37 residues) from different start points, we initiated AMT on a gridwork of poses and positions within the pore of S31 or N31 M2TM. We then simulated the configurational relaxations using three identical structures with different randomized initial velocities for each pose. As shown in Figure 6, AMT quickly adopts the three specific configurations, C1, C2, and C3, in both the S31 and N31 M2TM channels upon release.

The three primary configurations from PMFs, C1, C2, and C3, act as strong attractors. Most compelling is the attraction toward C1 in S31 for AMT, starting anywhere in  $6 \text{ Å} \leq \xi_z \leq 10 \text{ Å}$ . In N31, N-ward facing AMT molecules have a strong tendency to adopt C3 instead, i.e., to stay outward facing and hydrogen bonded to the N31 side-chain. This is demonstrated by both the green and cyan arrows originating in  $6 \text{ Å} \leq \xi_z \leq 10 \text{ Å}$ . Three other minor regions representing AMT configurations also appear: two are in the vicinity of the His37 side chains at  $(-2 \text{ Å}, -30^\circ)$  in S31 and  $(-1 \text{ Å}, -85^\circ)$  in N31, and the third is outside the channel at  $(15 \text{ Å}, 30^\circ)$  in N31 M2TM. Starting from  $\xi_z \approx 10 \text{ Å}$  and outward facing, AMT falls into the S31 channel, whereas it usually falls out of the N31 channel. Although this is consistent with a lower affinity of the N31 channel for amantadine, the evidence must be evaluated with

caution because of our current lack of knowledge of protein structure N-ward of Val27.

## DISCUSSION

The trends in AMT occupancy from the equilibration study, tilt angles from the steered MD study, and PMFs from the US/REMD studies are quite consistent. From these experiments, we draw attention to four important, novel observations: configurational preferences of AMT in M2TM, hydrogen-bonding of AMT in the M2TM pore, water molecule densities in the M2TM pore, and AMT binding free energies in the two channel types.

**Configurational Preferences of AMT in M2TM.** As AMT approaches the M2 pore, it must pass through the highly constricted Val27 sphincter. The largest free energy barrier to AMT entry in both channel types is near  $\xi_z = 12 \text{ Å}$  and  $\xi_\theta = 0^\circ$  (Figure 2), which indicates a large penalty for sideways-oriented AMT as it approaches and passes through the Val27 sphincter. The lowest free energy barriers in  $\xi_\theta$  for Val27 entry are near  $\xi_z \approx 12 \text{ Å}$  and  $\xi_\theta \approx \pm 60^\circ$ , which suggest AMT must travel through the Val27 facing either N-ward or C-ward with respect to the protein. Steered MD simulations of both S31 and N31 systems suggest a preference for outward entry through Val27, as AMT begins to adopt an outward orientation beginning at  $\xi_z = 22 \text{ Å}$  in all cases (Figure 3a,b). When visualizing trajectories, it is apparent that the  $\text{NH}_3^+$  group of AMT hydrogen bonds with water molecules N-ward of the Val27 sphincter, and the hydrophobic adamantane cage of AMT “backs in” through the valine side chains.

When AMT reaches  $\xi_z = 10 \text{ Å}$  and enters the M2TM pore, AMT orientation between S31 and N31 M2 begins to diverge. Three primary configurations of AMT within the M2TM pore are distinguished by free energy minima in the S31 and N31 PMFs (Figure 2), defined as C1, C2, and C3, as shown in the Results. Occupancy of AMT in each of these sites, as unrestrained AMT simulations suggest (Figure 6), correlates well with the PMFs: the highest density of equilibrated AMT in S31 M2TM is in C2 and C1 with reasonable density at C3, whereas equilibrated AMT in N31 M2TM has high occupancy in both C3 and C2 with diminutive density near C1. Steered MD simulations show that AMT has a strong tendency to orient C-ward in S31 M2TM before reaching  $\xi_z = 6 \text{ Å}$ , and in all runs, adopts C2 and C1 along the reaction coordinate (Figure 3). In the case of N31 M2TM, AMT tends to continue through the M2TM pore in an N-ward orientation with four out of five runs exploring C3 and the exceptional run exploring C2 and C1 in a manner similar to the S31 steered MD runs.

The simulations provide evidence for a strong tendency of AMT to adopt a C-ward configuration following pore entry in S31 M2TM. Nearly all unrestrained runs of AMT at  $\xi_z \geq 6 \text{ Å}$ , regardless of initial  $\xi_\theta$ , relax to C1 (Figure 6). When initiated at  $\xi_z < 6 \text{ Å}$ , AMT tends to adopt C2 when initiated at  $\xi_\theta \leq 0^\circ$  and C3 when AMT is initiated  $\xi_\theta > 0^\circ$ . In theory, C3 could be observed if AMT dropped deep into the channel pore ( $-2 \text{ Å} \leq \xi_z \leq 0 \text{ Å}$ ), flipped to face the N-termini, and then rose back into the channel N-ward facing. Such a course, however, is unlikely due to the depth of the free energy wells in the PMFs at C1 and C2 (Figure 2) and a lack of AMT escape from these configurations during equilibration (Figure 6).

The observation that C1 is rarely explored in Figure 6 is consistent with the lack of a free energy minimum near C1 in Figure 2. The N31 PMF instead features a sloping region between  $\xi_z = 7$  and  $3 \text{ Å}$  and  $\xi_\theta < 0^\circ$  (Figure 2), such that AMT

is not prone to persist high in the channel (in  $6 \text{ \AA} \leq \xi_z \leq 8 \text{ \AA}$ ; compare to Figure 6). In addition, the N31 PMF has a more prominent free energy ridge running from ( $10 \text{ \AA}$ ,  $0^\circ$ ) to ( $5 \text{ \AA}$ ,  $40^\circ$ ), which may prevent AMT rotation between the two extremes until it drops deeper into the channel. Furthermore, the free energy barrier in  $\xi_\theta$  separating C2 and C3, i.e., the saddle in  $2 \text{ \AA} \leq \xi_z \leq 4 \text{ \AA}$ , is smaller in magnitude in the N31 PMF than in the S31 PMF, which affords AMT more flexibility in orientation when between 2 and 4  $\text{\AA}$  in N31 M2TM. This flexibility is observed in the steered MD simulations, as AMT explores more of  $\xi_\theta$  in N31 than in S31 M2TM following pore entry (see Figure 3a,b).

Interestingly, the PMF does little to explain why AMT tends to adopt C1 over C3 when AMT enters the pore of S31 M2TM. A C-ward slope between  $\xi_z = 6$  and  $8 \text{ \AA}$  is obvious; however, the free energy gradient near  $\xi_z = 10 \text{ \AA}$  and  $\xi_\theta < -70^\circ$  points in the direction of C3. One possible factor is that the influence of water molecules on AMT entry is underestimated in the US/REMD study because water molecules overlapping AMT are deleted at every umbrella window, unlike the steered MD study in which water molecules must be displaced as AMT is translated along the channel axis into the pore. These water molecules occupying the M2TM pore might cause AMT to spend more time N-ward in the pore upon entry until empty space exists deeper in the pore, perhaps as water molecules diffuse out the C-terminal end of the protein. Held in the N-ward region of the pore, AMT would likely adopt C1 until space deeper in the channel is available, at which point it would either remain in C1 or adopt C2.

The distinct free energy minima in the S31 and N31 PMFs, as well as the lack of minima near  $\xi_z \approx 6.75 \text{ \AA}$  and  $\xi_\theta < -70^\circ$  in N31 M2TM, correspond with observations about ammonium and AMT amine localization in previous work.<sup>9,14</sup> Wang et al. (2013)<sup>3</sup> illustrate that AMT adopts C1 in S31 M2TM, according to Figure 3E in their study,<sup>3</sup> in agreement with our current and previous MD simulations<sup>8</sup> of AMT in the ssNMR structure. Our previous 1-dimensional PMFs also agree with those of Gianti et al. (2015),<sup>14</sup> in which they show, using the homologue of an S31 M2TM crystal structure, that the AMT animum localizes to the plane of the N31 C- $\alpha$ 's, which corresponds both to C1 and to the 2KQT configuration. Curiously, both 1-dimensional PMFs show a preference for AMT with a  $\xi_z$  equivalent to C2 over C1 in S31 M2TM, which we suspect is an artifact of undersampling of  $\xi_\theta$  in the pore and is addressed with the 2-dimensional PMFs of the present study, where C1 is more favorable than C2 by  $-1.5 \text{ kcal/mol}$ .

The 2-dimensional PMFs demonstrate the diverse topology encountered by AMT when changing orientation and provide an explanation for the divergent orienting behavior of AMT in both S31 and N31 M2TM. Furthermore, escape of AMT from the M2TM pore to metastable sites beyond the Val27 residues is only observed in runs of AMT in N31 M2TM, and the free energy of AMT binding in N31 is more positive than in S31 M2TM, both of which indicate a greater rate constant for AMT escape from the N31 pore than the S31 pore on a long time scale.

**Hydrogen-Bonding in the M2TM Pore.** Hydrogen-bonding of AMT, according to our simulations, helps to address why AMT adopts specific tilt angles in the M2TM pore. Hydrogen atoms of the AMT  $\text{NH}_3^+$  group can hydrogen bond with certain pore-lining acceptors, including the backbone carbonyl oxygen of Ala30, the hydroxyl oxygen of the Ser31 side chain (O- $\delta$ ), and the carboxamide oxygen of the Asn31

side chain (O- $\gamma$ ). Also, the AMT  $\text{NH}_3^+$  group frequently hydrogen bonds with nearby water molecules whether AMT is inside or outside of the M2TM pore. These hydrogen bonds influence how AMT orients and where it positions when in the M2TM pore.

In none of our steered MD simulations did the  $\text{NH}_3^+$  group of AMT exhibit significant hydrogen bonding with the carbonyl of Ala30, but significant bonding with the Ser31 and Asn31 side-chain oxygens was observed. When AMT is within  $2 \text{ \AA} \leq \xi_z \leq 8 \text{ \AA}$  in N31 steered MD simulations, at least one Asn31 side-chain O- $\gamma$  is typically within hydrogen-bonding length of the AMT  $\text{NH}_3^+$  (Figure 5). In S31 steered MD simulations, some Ser31 side-chain O- $\delta$  hydrogen bonding to the AMT  $\text{NH}_3^+$  is observed, but these interactions are sporadic and typically short-lived. In addition to protein interactions, AMT  $\text{NH}_3^+$  hydrogen bonding with the oxygen of water molecules is readily observed when visualizing steered MD trajectories. When near C1 and C2, interactions between the AMT  $\text{NH}_3^+$  group and pore water molecules are ubiquitous, and hydrogen-bonding of the  $\text{NH}_3^+$  hydrogen atoms to both Asn-31 O- $\gamma$  and water are observed when it adopts C3 in N31 M2TM (Figure 3).

The observed hydrogen-bonding of AMT in M2TM provides one significant driving force for specific AMT orientations in the M2TM pore. In N31 M2TM, AMT is typically tilted N-ward and within hydrogen-bonding range of at least one Asn31 O- $\gamma$  when within  $2 \text{ \AA} \leq \xi_z \leq 8 \text{ \AA}$  in N31 M2TM, whereas it forms few hydrogen bonds with S31 M2TM over the same region (Figure S8). Also, the hydrogen-bond distances observed for the nitrogen of AMT  $\text{NH}_3^+$  to Asn31 O- $\gamma$  are slightly shorter than those observed for Ser31 O- $\delta$ , indicating that the Asn31 interaction is stronger than the Ser31 interaction. Thus, AMT orients toward the most polar regions of the pore: it maintains an N-ward orientation after N31 M2TM pore entry, at least on a short time scale, in order to hydrogen bond with Asn-31 O- $\gamma$  and nearby water molecules, and it adopts a C-ward orientation in S31 M2TM to interact with pore water molecules near the His37 cluster.

**Water Molecules in the M2TM Pore.** The S31N mutation converts a small polar amino acid, with an experimental neutral pH side-chain hydrophobicity index of  $-5$ , into a very hydrophilic amino acid with a hydrophobicity index of  $-28$ .<sup>43</sup> As a result, the Asn31 side chains attract water through the Val27 side chain cluster better than those of Ser31. When no AMT is bound, water tends to occupy the pore in a similar fashion between S31 and N31 M2TM (see Figures S4 and S5). However, water molecules are typically absent in the region above AMT and below the Val sphincter when AMT is at C2 or C3 in S31 M2TM, and water molecules persist regardless of AMT orientation or position in the N31 channel (Figure 4 and Figure S7). The persistence of water in this region in N31 M2TM likely accelerates water-wire formation, and therefore proton conductance, and increases the probability of AMT escape as water molecules are available to draw AMT out of the channel when it is oriented outward. The vacancy in this region profoundly influences the distance separating water molecules on opposite ends of AMT, which is a rough indicator of how effectively M2 can conduct protons across the membrane, and patterns in water density and separation emerge with varying combinations of  $\xi_z$  and  $\xi_\theta$  of AMT in M2TM.

In steered MD simulations, AMT tends to induce the largest separation in water molecules in S31 M2TM overall, especially

when constrained near  $3 \text{ \AA} \leq \xi_z \leq 7 \text{ \AA}$ , where it tends to orient inward (Figure 3c,d). In this region, water separation ranges from 6 to 11 Å along the channel axis. Although the highest separation and lowest deviation is observed in  $4 \text{ \AA} \leq \xi_z \leq 6 \text{ \AA}$ , this area lies directly between C1 and C2, which has little occupancy as determined in other S31 simulations (see Figures 2 and 6), and the area near C2 has a higher standard deviation in the level of water separation between runs, corresponding to the higher deviation in observed  $\xi_\theta$  between runs (see Figure 3). In the case of N31 steered MD simulations, AMT induces no more than a 5 Å water separation in either of its most-occupied configurations. Therefore, AMT in S31 M2TM in C1, just N-ward of  $\xi_z = 6 \text{ \AA}$ , produces the most consistent water separation.

In the US/REMD experiment, average water density is low near AMT in all cases, but when AMT is constrained to  $\xi_z = 6 \text{ \AA}$  and oriented C-ward in S31 M2TM, extremely low water density (approaching  $0 \text{ g/mol/\AA}^3$ ) persists from 5 to 12 Å along the channel axis (Figure S7). Low water density persists only from 5 to 9 Å in the case of N-ward oriented AMT with the same  $\xi_z$  in S31 M2TM. In N31 M2TM, AMT produces nearly indistinguishable water densities whether oriented C- or N-ward with the exception of an exclusive, low-density region when AMT, oriented C-ward, is restrained to  $\xi_z = -2$  to  $0 \text{ \AA}$ . This area has visible occupancy according to the results of the AMT-equilibration studies (see Figure 6), but nearby areas of substantially lower free energy would prevent reliable occupancy in such a configuration on a longer time scale (see Figure 2).

As expected, when unrestrained AMT is left to equilibrate for 200 ns in S31 M2TM, initiated at C1, it has the most sturdy block of proton conductance (Figure S9). Unrestrained AMT in N31 M2TM initiated at C3 provides substantial inhibition of nearby water density, but water density never reaches zero along the channel axis unlike AMT in S31 M2TM. Our volume-density maps indicate water density along the channel axis may be sufficient to allow Grotthus proton conductivity because the isosurface threshold of  $10^{-5} \text{ g/mL}$  indicates continuity in water density in the N31 channel. Therefore, AMT, provided it does not escape the pore, may not be rate-limiting when bound to N31 M2TM in C3, and quasi-normal proton transport through the channel may be achieved.

Together, these results suggest that AMT induces a persistent, dry region in S31 M2, extending well beyond AMT's geometrical dimensions, in which water molecules are sparse and distant from each other in opposite directions of AMT when it adopts C1 or, to a lesser extent, C2. Furthermore, the PMFs suggest AMT is stable in these blocking configurations. AMT in N31 M2 exhibits no extended water separation, even when at different configurations. Although some regions show evidence of notable distance between water molecules for AMT in N31 M2, the configurations in these regions are less stable according to the PMFs (compare Figure 2b to 2a). Consequently, increased probability of deviations in AMT tilt would result in periods of higher water density and lower molecular separation that we propose would suffice to allow for occasional proton transport in the experimentally observed range of  $\sim 300/\text{s}$ .<sup>44</sup>

**Global Free Energy Minimum.** A comparison of the global minima between AMT S31 and N31 M2TM reveals that AMT binds more tightly to the S31 M2TM pore. The C1 site in S31 M2TM has a free energy minimum of  $-23.5 \text{ kcal/mol}$ , whereas the C2 site in N31 M2TM is  $-15.5 \text{ kcal/mol}$ .

Without detailed knowledge of the N-terminus of M2, we project that the entry path for the full length protein and its S31N mutation are similar as the mutation is confined to one amino acid that is fairly deep in the channel. The free energy barrier along this path is also likely similar in the two proteins; therefore, the rate constant for entry is probably similar for the two. The dissociation constant and rate constant for exit should be higher in N31, as is expected from experimental EC50s and washout times<sup>45</sup> based on the difference between the global free energy minima in the channel of  $8.0 \text{ kcal/mol}$ . Furthermore, in the steered MD simulations, AMT is attracted first to the C3 site, which, in spite of hydrogen bonds to N31 side chains, is much higher in energy ( $-7.3 \text{ kcal/mol}$ ) and would serve as a stage for returning back out of the channel. The origin of this binding energy difference in the two channels has not yet been explored.

Binding free energies can be compared to those found in other studies. Using different channel models, His37 protonation states, force fields, methodology, and approximate values for the energy of AMT binding to the intrachannel M2 binding site relative to bulk water have been previously reported as  $-0.9$ ,<sup>20</sup>  $-9.5$  (rimantadine),<sup>13</sup>  $-21.0$ ,<sup>46</sup> and  $-30.7$ <sup>47</sup> kcal/mol, respectively. From a dissociation constant of  $0.3 \mu\text{M}$ ,<sup>48</sup> one might expect a free energy of binding near  $-RT \ln K_d^{-1} = -9 \text{ kcal/mol}$ . Here, the use of the solid state NMR structure for the AMT-M2 complex, of an all-atom force field, explicit water, neutral His37 imidazoles, extensive replica exchange sampling, careful comparison to the reference state, and examination of the 2D reaction coordinate are all factors that could impact the accuracy of the calculated binding energy. In our opinion, we have optimized the accuracy for all of these factors, but the computed energies reported in Figure 2 are more negative by  $13 \text{ kcal/mol}$ . Protein backbone restraints could overly stabilize the protein, or the short-tailed DMPC environment used in the 2KQT structure determination could influence helix tilt,<sup>49,50</sup> perhaps leading to deeper free-energy wells and higher free-energy barriers.

The principal structural difference between the bound states for the two channels is the structure of water in the entryway. With AMT in C2 of N31, the entryway is filled with water, presumably attracted by hydrogen bonding to the N31 side chains, whereas with AMT in C1 (or C2) of S31, the entryway is vacant, presumably due to reduced hydrogen-bonding capacity of the S31 side chain. In a previous study, we suggested that AMT may bind without blocking in N31 M2, slipping deeper into the channel where water could bypass the drug laterally on one side or another and provide a pathway for Grotthus transport of protons.<sup>8</sup> Here, we used the same M2TM structure (an average of the 2KQT models with mild backbone constraints in a DMPC bilayer with  $150 \text{ mM NaCl}$  comprised of TIP3 water) and its S31N homology model to confirm, expand, and in some ways correct the concepts explored there and in other prior simulation studies of M2. We continued to assume that AMT would have persistent protonation in the channel and that it would drive deprotonation of the His37 cluster. Here, however, we dismissed the concept explored in the free dynamics simulations there that  $\text{Cl}^-$  might be caught in the central cavity with the drug on the grounds that, even with the charged AMT or charged selectivity filter, such events would seem unlikely given the sparsity of water in the channel ( $\sim 20$  molecules in the unbound state and  $8-15$ , depending on AMT position, in the bound state) compared to the density of  $\text{Cl}^-$  in the bath (1 ion per 367 water molecules). This decision

was also informed by previous assessments of the free energy profile for  $\text{Cl}^-$  transport through the apo-M2 protein at different protonation states of the selectivity filter.<sup>51</sup>

Although inward-projecting AMT in S31 M2TM yielded a strong water vacancy between the drug and the V27 side chains, this pocket was consistently filled with water in the N31 M2TM when the AMT was outward projecting, as might be expected due to the charge on the drug  $\text{NH}_3^+$ . However, it was also consistently filled when AMT was inward facing, indicating that hydrogen bonding of water molecules with the N31 side chains is a compelling driving force for hydration of this otherwise hydrophobically bounded region. This level of detail may well be specific for the empirical model of water and side chain used here, but if it persists with more complete force fields, it could indicate that lateral water wires spanning the drug, though rare, could still be more common in the N31 channel than in the S31 channel.

However, probably of greater importance is the novel assessment of the 2D umbrella sampling profile, which with imposed periodicity on the water bath free energy for the two sides of the membrane, allows us for the first time to observe that the binding energy for AMT in N31 M2TM is significantly less negative than in S31 M2TM. Whether binding without block or weaker binding is more important for AMT in N31 M2TM can be determined with electrophysiology dose-response and washout experiments. For instance, binding without block should not be amenable to washout, whereas weak binding that yields partial block at high drug concentrations should lead to partial block that is readily washed out by perfusion with drug-free solution and completely recovered by changing perfusion back to the high drug concentration. In fact, washout experiments have shown that Udorn M2 (S31N) is partially blocked by amantadine, and washes out readily, whereas native Udorn M2 is fully blocked by AMT and does not wash out on the 30 min time scales.<sup>45</sup> If this finding is general for all types of M2, and if further increases of [AMT] for the N31 channel result in complete block, one would conclude that N31 M2 has low binding affinity for AMT rather than binding without block. Hence, distinguishing between the two models of block proposed here and previously<sup>8</sup> should be readily accomplished experimentally.

## CONCLUSIONS

Simulations of AMT in the S31 and N31 M2TM demonstrate the significance of AMT tilt and position on its ability to prevent proton transport in the M2 channel. AMT induces a compelling dry region in S31 M2TM, which persists in its principal binding configuration, C1, in which it is oriented toward the C-terminus with the adamantane cage just N-ward of the Ser31 C- $\alpha$ . Such a dry region does not exist when AMT is oriented toward the N-terminus of S31 M2TM or in the N31 pore at any orientation. However, the water density around the drug is actually very modest at all drug positions in the channel. Rather than binding without block, we suggest here that AMT binding should be substantially weaker in the N31 pore due to lower free energy well depth for AMT's primary binding configurations. Electrophysiological washout experiments should allow us to distinguish which of these two mechanisms, binding without block or weakened binding, is primarily responsible for weak AMT block of proton transport in M2 N31.

## ASSOCIATED CONTENT

### Supporting Information

The Supporting Information is available free of charge on the ACS Publications website at DOI: 10.1021/acs.jpcc.5b05808.

Hydration statistics of Apo-M2, expanded PMFs, water density from 2D US/REMD simulations, hydrogen-bonding behavior of pore-bound AMT, and mass-weighted volume density data (PDF)

## AUTHOR INFORMATION

### Corresponding Author

\*E-mail: david\_busath@byu.edu.

### Notes

The authors declare no competing financial interest.

## ACKNOWLEDGMENTS

The authors are grateful to the Fulton Supercomputing Lab at Brigham Young University for generous compute time and to Stephen Cluff for support with analysis. The work was supported by grants from NIH (AI 23007 to Timothy Cross) and Chiesi Hellas to A.K.

## REFERENCES

- (1) Kochanek, K. D.; Murphy, S. L.; Xu, J.; Arias, E., Mortality in the United States, 2013. National Center for Health Statistics. U.S. Department of Health and Human Services: Hyattsville, MD, 2014; pp 1–8.
- (2) Davies, W. L.; Grunert, R. R.; Haff, R. F.; McGahen, J. W.; Neumayer, E. M.; Paulshock, M.; Watts, J. C.; Wood, T. R.; Hermann, E. C.; Hoffmann, C. E. Antiviral Activity of 1-Adamantanamine (Amantadine). *Science* **1964**, *144*, 862–3.
- (3) Wang, J.; Wu, Y.; Ma, C.; Fiorin, G.; Pinto, L. H.; Lamb, R. A.; Klein, M. L.; Degrado, W. F. Structure and Inhibition of the Drug-Resistant S31N Mutant of the M2 Ion Channel of Influenza A Virus. *Proc. Natl. Acad. Sci. U. S. A.* **2013**, *110*, 1315–20.
- (4) Kolocouris, A.; Tzitzoglaki, C.; Johnson, F. B.; Zell, R.; Wright, A. K.; Cross, T. A.; Tietjen, I.; Fedida, D.; Busath, D. D. Amino-adamantanes with Persistent *in vitro* Efficacy against H1N1 (2009) Influenza A. *J. Med. Chem.* **2014**, *57*, 4629–39.
- (5) Rey-Carrizo, M.; Torres, E.; Ma, C.; Barniol-Xicota, M.; Wang, J.; Wu, Y.; Naesens, L.; DeGrado, W. F.; Lamb, R. A.; Pinto, L. H.; et al. 3-Azatetracyclo[5.2.1.1(5,8).0(1,5)]Undecane Derivatives: From Wild-Type Inhibitors of the M2 Ion Channel of Influenza A Virus to Derivatives with Potent Activity against the V27A Mutant. *J. Med. Chem.* **2013**, *56*, 9265–74.
- (6) Zhao, X.; Jie, Y.; Rosenberg, M. R.; Wan, J.; Zeng, S.; Cui, W.; Xiao, Y.; Li, Z.; Tu, Z.; Casarotto, M. G.; et al. Design and Synthesis of Pinanamine Derivatives as Anti-Influenza A M2 Ion Channel Inhibitors. *Antiviral Res.* **2012**, *96*, 91–9.
- (7) Fiore, A. E.; Fry, A.; Shay, D.; Gubareva, L.; Bresee, J. S.; Uyeki, T. M. Antiviral Agents for the Treatment and Chemoprophylaxis of Influenza. *Morbidity and Mortality Weekly Report*, 2011.
- (8) Gleed, M. L.; Busath, D. D. Why Bound Amantadine Fails to Inhibit Proton Conductance According to Simulations of the Drug-Resistant Influenza A M2 (S31N). *J. Phys. Chem. B* **2015**, *119*, 1225–31.
- (9) Qin, G.; Yu, K.; Shi, T.; Luo, C.; Li, G.; Zhu, W.; Jiang, H. How Does Influenza Virus A Escape from Amantadine? *J. Phys. Chem. B* **2010**, *114*, 8487–93.
- (10) Gkeka, P.; Eleftheratos, S.; Kolocouris, A.; Courmia, Z. Free Energy Calculations Reveal the Origin of Binding Preference for Aminoadamantane Blockers of Influenza A/M2tm Pore. *J. Chem. Theory Comput.* **2013**, *9*, 1272–1281.
- (11) Wu, Y.; Canturk, B.; Jo, H.; Ma, C.; Gianti, E.; Klein, M. L.; Pinto, L. H.; Lamb, R. A.; Fiorin, G.; Wang, J.; et al. Flipping in the

Pore: Discovery of Dual Inhibitors That Bind in Different Orientations to the Wild-Type Versus the Amantadine-Resistant S31N Mutant of the Influenza A Virus M2 Proton Channel. *J. Am. Chem. Soc.* **2014**, *136*, 17987–95.

(12) Wang, J.; Ma, C.; Fiorin, G.; Carnevale, V.; Wang, T.; Hu, F.; Lamb, R. A.; Pinto, L. H.; Hong, M.; Klein, M. L.; et al. Molecular Dynamics Simulation Directed Rational Design of Inhibitors Targeting Drug-Resistant Mutants of Influenza A Virus M2. *J. Am. Chem. Soc.* **2011**, *133*, 12834–12841.

(13) Alhadeff, R.; Assa, D.; Astrahan, P.; Krugliak, M.; Arkin, I. T. Computational and Experimental Analysis of Drug Binding to the Influenza M2 Channel. *Biochim. Biophys. Acta, Biomembr.* **2014**, *1838*, 1068–73.

(14) Gianti, E.; Carnevale, V.; DeGrado, W. F.; Klein, M. L.; Fiorin, G. Hydrogen-Bonded Water Molecules in the M2 Channel of the Influenza A Virus Guide the Binding Preferences of Ammonium-Based Inhibitors. *J. Phys. Chem. B* **2015**, *119*, 1173–83.

(15) Acharya, R.; Carnevale, V.; Fiorin, G.; Levine, B. G.; Polishchuk, A. L.; Balannik, V.; Samish, I.; Lamb, R. A.; Pinto, L. H.; DeGrado, W. F.; et al. Structure and Mechanism of Proton Transport through the Transmembrane Tetrameric M2 Protein Bundle of the Influenza A Virus. *Proc. Natl. Acad. Sci. U. S. A.* **2010**, *107*, 15075–80.

(16) Cady, S. D.; Schmidt-Rohr, K.; Wang, J.; Soto, C. S.; Degrado, W. F.; Hong, M. Structure of the Amantadine Binding Site of Influenza M2 Proton Channels in Lipid Bilayers. *Nature* **2010**, *463*, 689–92.

(17) Cady, S. D.; Wang, J.; Wu, Y.; DeGrado, W. F.; Hong, M. Specific Binding of Adamantane Drugs and Direction of Their Polar Amines in the Pore of the Influenza M2 Transmembrane Domain in Lipid Bilayers and Dodecylphosphocholine Micelles Determined by NMR Spectroscopy. *J. Am. Chem. Soc.* **2011**, *133*, 4274–4284.

(18) Intharathep, P.; Laohpongspaisan, C.; Rungrotmongkol, T.; Loisuangsin, A.; Malaisree, M.; Decha, P.; Aruksakunwong, O.; Chuenpennit, K.; Kaiyawet, N.; Sompornpisut, P.; et al. How Amantadine and Rimantadine Inhibit Proton Transport in the M2 Protein Channel. *J. Mol. Graphics Modell.* **2008**, *27*, 342–348.

(19) Yi, M.; Cross, T. A.; Zhou, H.-X. A Secondary Gate as a Mechanism for Inhibition of the M2 Proton Channel by Amantadine. *J. Phys. Chem. B* **2008**, *112*, 7977–7979.

(20) Leonov, H.; Astrahan, P.; Krugliak, M.; Arkin, I. T. How Do Aminoadamantanes Block the Influenza M2 Channel, and How Does Resistance Develop? *J. Am. Chem. Soc.* **2011**, *133*, 9903–11.

(21) MacKerell, A. D.; Bashford, D.; Bellott, D.; Dunbrack, R. L.; Evanseck, J. D.; Field, M. J.; Fischer, S.; Gao, J.; Guo, H.; Ha, S.; et al. All-Atom Empirical Potential for Molecular Modeling and Dynamics Studies of Proteins. *J. Phys. Chem. B* **1998**, *102*, 3586–3616.

(22) Klauda, J. B.; Venable, R. M.; Freites, J. A.; O'Connor, J. W.; Tobias, D. J.; Mondragon-Ramirez, C.; Vorobyov, I.; MacKerell, A. D.; Pastor, R. W. Update of the CHARMM All-Atom Additive Force Field for Lipids: Validation on Six Lipid Types. *J. Phys. Chem. B* **2010**, *114*, 7830–7843.

(23) Jorgensen, W. L.; Chandrasekhar, J.; Madura, J. D.; Impey, R. W.; Klein, M. L. Comparison of Simple Potential Functions for Simulating Liquid Water. *J. Chem. Phys.* **1983**, *79*, 926–935.

(24) Yu, W.; He, X.; Vanommeslaeghe, K.; MacKerell, A. D., Jr. Extension of the CHARMM General Force Field to Sulfonamide-Containing Compounds and Its Utility in Biomolecular Simulations. *J. Comput. Chem.* **2012**, *33*, 2451–68.

(25) Vanommeslaeghe, K.; Hatcher, E.; Acharya, C.; Kundu, S.; Zhong, S.; Shim, J.; Darian, E.; Guvench, O.; Lopes, P.; Vorobyov, I.; et al. CHARMM General Force Field: A Force Field for Drug-Like Molecules Compatible with the Charmm All-Atom Additive Biological Force Fields. *J. Comput. Chem.* **2010**, *31*, 671–90.

(26) Vanommeslaeghe, K.; MacKerell, A. D., Jr. Automation of the Charmm General Force Field (CGENFF) I: Bond Perception and Atom Typing. *J. Chem. Inf. Model.* **2012**, *52*, 3144–54.

(27) Vanommeslaeghe, K.; Raman, E. P.; MacKerell, A. D., Jr. Automation of the CHARMM General Force Field (CGENFF) II: Assignment of Bonded Parameters and Partial Atomic Charges. *J. Chem. Inf. Model.* **2012**, *52*, 3155–68.

(28) Essmann, U.; Perera, L.; Berkowitz, M. L.; Darden, T.; Lee, H.; Pedersen, L. G. A Smooth Particle Mesh Ewald Method. *J. Chem. Phys.* **1995**, *103*, 8577–8593.

(29) Ryckaert, J.-P.; Ciccotti, G.; Berendsen, H. J. C. Numerical Integration of the Cartesian Equations of Motion of a System with Constraints: Molecular Dynamics of N-Alkanes. *J. Comput. Phys.* **1977**, *23*, 327–341.

(30) Green, D. A. A Colour Scheme for the Display of Astronomical Intensity Images. *Bulletin of the Astronomical Society of India* **2011**, *39*, 289–295.

(31) Jo, S.; Kim, T.; Iyer, V. G.; Im, W. harrm-Gui: A Web-Based Graphical User Interface for CHARMM. *J. Comput. Chem.* **2008**, *29*, 1859–65.

(32) Wu, E. L.; Cheng, X.; Jo, S.; Rui, H.; Song, K. C.; Dávila-Contreras, E. M.; Qi, Y.; Lee, J.; Monje-Galvan, V.; Venable, R. M.; et al. CHARMM-GUI Membrane Builder: Toward Realistic Biological Membrane Simulations. *J. Comput. Chem.* **2014**, *35*, 1997–2004.

(33) Hu, J.; Fu, R.; Nishimura, K.; Zhang, L.; Zhou, H. X.; Busath, D. D.; Vijayvergiya, V.; Cross, T. A. Histidines, Heart of the Hydrogen Ion Channel from Influenza A Virus: Toward an Understanding of Conductance and Proton Selectivity. *Proc. Natl. Acad. Sci. U. S. A.* **2006**, *103*, 6865–70.

(34) Williams, J. K.; Tietze, D.; Wang, J.; Wu, Y.; DeGrado, W. F.; Hong, M. Drug-Induced Conformational and Dynamical Changes of the S31N Mutant of the Influenza M2 Proton Channel Investigated by Solid-State NMR. *J. Am. Chem. Soc.* **2013**, *135*, 9885–9897.

(35) Sharma, M.; Yi, M.; Dong, H.; Qin, H.; Peterson, E.; Busath, D. D.; Zhou, H.-X.; Cross, T. A. Insight into the Mechanism of the Influenza A Proton Channel from a Structure in a Lipid Bilayer. *Science* **2010**, *330*, 509–512.

(36) Lomize, M. A.; Lomize, A. L.; Pogozheva, I. D.; Mosberg, H. I. OPM: Orientations of Proteins in Membranes Database. *Bioinformatics* **2006**, *22*, 623–5.

(37) Brooks, B. R.; Brooks, C. L., 3rd; Mackerell, A. D., Jr.; Nilsson, L.; Petrella, R. J.; Roux, B.; Won, Y.; Archontis, G.; Bartels, C.; Boresch, S.; et al. CHARMM: The Biomolecular Simulation Program. *J. Comput. Chem.* **2009**, *30*, 1545–614.

(38) Koynova, R.; Caffrey, M. Phases and Phase Transitions of the Phosphatidylcholines. *Biochim. Biophys. Acta, Rev. Biomembr.* **1998**, *1376*, 91–145.

(39) Phillips, J. C.; Braun, R.; Wang, W.; Gumbart, J.; Tajkhorshid, E.; Villa, E.; Chipot, C.; Skeel, R. D.; Kalé, L.; Schulten, K. Scalable Molecular Dynamics with NAMD. *J. Comput. Chem.* **2005**, *26*, 1781–1802.

(40) Murata, K.; Sugita, Y.; Okamoto, Y. Free Energy Calculations for DNA Base Stacking by Replica-Exchange Umbrella Sampling. *Chem. Phys. Lett.* **2004**, *385*, 1–7.

(41) Fiorin, G.; Klein, M. L.; Hénin, J. Using Collective Variables to Drive Molecular Dynamics Simulations. *Mol. Phys.* **2013**, *111*, 3345–3362.

(42) Grossfield, A. *Wham: The Weighted Histogram Analysis Method*, 2.0.9.

(43) Monera, O. D.; Sereda, T. J.; Zhou, N. E.; Kay, C. M.; Hodges, R. S. Relationship of Sidechain Hydrophobicity and  $\alpha$ -Helical Propensity on the Stability of the Single-Stranded Amphipathic  $\alpha$ -Helix. *J. Pept. Sci.* **1995**, *1*, 319–329.

(44) Lin, T. I.; Schroeder, C. Definitive Assignment of Proton Selectivity and Attoampere Unitary Current to the M2 Ion Channel Protein of Influenza A Virus. *J. Virol.* **2001**, *75*, 3647–56.

(45) Stouffer, A. L.; Ma, C.; Cristian, L.; Ohigashi, Y.; Lamb, R. A.; Lear, J. D.; Pinto, L. H.; DeGrado, W. F. The Interplay of Functional Tuning, Drug Resistance, and Thermodynamic Stability in the Evolution of the M2 Proton Channel from the Influenza a Virus. *Structure* **2008**, *16*, 1067–76.

(46) Gu, R.; Liu, L. A.; Wei, D. Drug Inhibition and Proton Conduction Mechanisms of the Influenza A M2 Proton Channel. *Adv. Exp. Med. Biol.* **2015**, *827*, 205–26.

(47) Nguyen, H.; Le, L. Steered Molecular Dynamics Approach for Promising Drugs for Influenza A Virus Targeting M2 Channel Proteins. *Eur. Biophys. J.* **2015**, *44*, 447.

(48) Wang, C.; Takeuchi, K.; Pinto, L. H.; Lamb, R. A. Ion Channel Activity of Influenza A Virus M2 Protein: Characterization of the Amantadine Block. *J. Virol.* **1993**, *67*, 5585–5594.

(49) Duong-Ly, K. C.; Nanda, V.; Degrado, W. F.; Howard, K. P. The Conformation of the Pore Region of the M2 Proton Channel Depends on Lipid Bilayer Environment. *Protein Sci.* **2005**, *14*, 856–61.

(50) Hu, F.; Luo, W.; Cady, S. D.; Hong, M. Conformational Plasticity of the Influenza A M2 Transmembrane Helix in Lipid Bilayers under Varying pH, Drug Binding, and Membrane Thickness. *Biochim. Biophys. Acta, Biomembr.* **2011**, *1808*, 415–23.

(51) Mustafa, M.; Henderson, D. J.; Busath, D. D. Free-Energy Profiles for Ions in the Influenza M2-TMD Channel. *Proteins: Struct., Funct., Genet.* **2009**, *76*, 794–807.